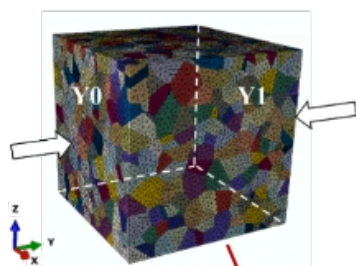


- Numerical-experimental multi-scale study of Mg alloy AZ31B deformation by FEA & diffraction
- CPFEM model experimentally validated at all scales: macro-(Type I)/micro-(Type II)/nano-(Type III)
- Calibrated Model parameters: CRSS for detwinning of 23 MPa, for twinning of 46.5 MPa
- Type I validation: model prediction matched to the macroscopic stress-strain response
- Type II validation: model predicted transition between plastic deformation modes (slip, twinning and detwinning), and matched peak intensities from *in situ* XRD experiments
- Type III validation: intra-granular stress statistics is revealed, but match to real twin morphology from *in situ* EBSD needs to be improved

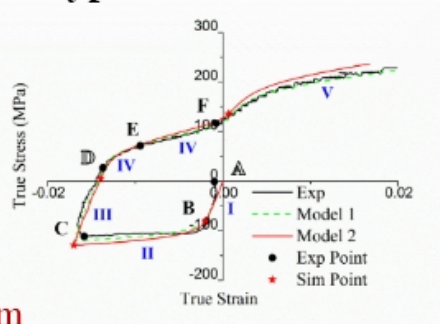
CFPEM →
(slip, twin-detwin)

Multi-Scale Validation

← **Experiment**

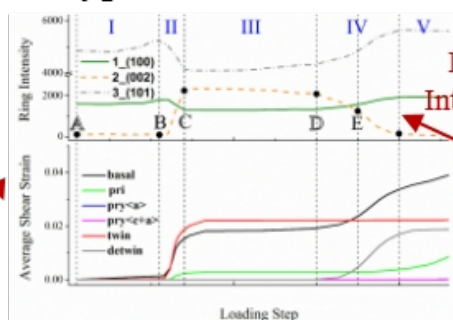


Type I: macro-scale



**System
Activity**

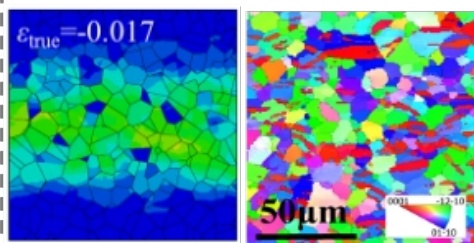
Type II: micro-scale



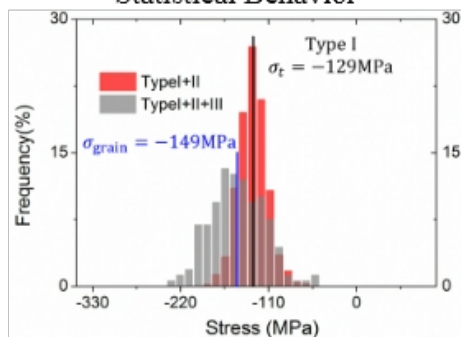
**Twin
Morphology**

Type III: nano-scale

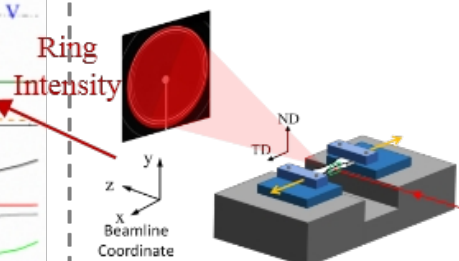
Local Behavior



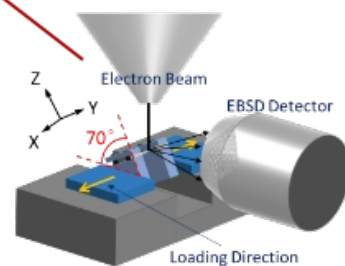
Statistical Behavior



In Situ XRD



**Twin
Morphology** *In Situ EBSD*



Multi-Scale Mechanisms of Twinning-Detwinning in Magnesium AZ31B Alloy Simulated by Crystal Plasticity Modeling and Validated via *In Situ* Synchrotron XRD and *In Situ* SEM-EBSD

Hongjia Zhang^{a,c}, Antoine Jérusalem^a, Enrico Salvati^a, Chrysanthi Papadaki^a, Kai Soon Fong^b, Xu Song^b, Alexander M. Korsunsky^{a,*}

^a Department of Engineering Science, University of Oxford, Oxford, UK

^b Singapore Institute of Manufacturing Technology, Singapore

^c College of Intelligence Science and Technology, National University of Defense Technology, China

Abstract

We present a combined experimental and numerical study that provides the understanding of deformation mechanisms and stresses in Mg AZ31B alloy across the scales, from macro-scale (Type I) to micro- (inter-granular, Type II) and nano-scale (intra-granular, Type III). The combination of *in situ* synchrotron X-ray diffraction (XRD), *in situ* electron backscattered diffraction (EBSD) and crystal plasticity finite element (CPFE) modeling of crystal slip and twinning/detwinning was employed. The crystal rotation observed directly in the XRD and EBSD experiments revealed the onset and completion of the twinning/detwinning processes during *in situ* cyclic compression-tension loading. It also allowed reliable calibration of the key model parameters, in particular critical resolved shear stress (CRSS) of detwinning. The validation of the model was performed at distinct different scales corresponding to all stress types. Direct comparison with the data from the loading device provided the confirmation of the model validity in terms of correct description of the macroscopic stress-strain response (Type I stresses). The calibration led to the CRSS detwinning value of 23 MPa, and twinning of 46.5 MPa. At the inter-granular micro-scale (Type II stresses), the model satisfactorily predicted the transition between different plastic deformation modes (slip, twinning and detwinning), as confirmed by the comparison with peak intensities in XRD experiments. For the intra-

granular (nano-scale) Type III stresses, it was concluded that the model was also valid at the level of statistical description (rather than local behavior). Namely, it has not been possible to predict correctly the real morphology of the twins observed in EBSD experiments.

Keywords: Crystal Plasticity Finite Element Model, Twinning-Detwinning, Multi-Scale Validation, *in situ* EBSD, *in situ* XRD

1. Introduction

Magnesium alloys have been extensively studied in the recent decades as structural materials for advanced applications (Pandey et al., 2015; Wang and Agnew, 2016) thanks to their high specific strength and lowest density (1.738 g/cm^3) (Avedesian and Baker, 1999) among all structural metals. Due to a lack of independent slip systems at ambient temperature (Groves and Kelly, 1963; Taylor, 1938), deformation twinning plays a critical role in plastic deformation of these metals by accommodating the strain along the c -axis of the hexagonal unit cell (Cui et al., 2017; Khan et al., 2011; Ma et al., 2012). Unlike slip which involves incremental shear and gradual local change of lattice orientation, deformation twinning causes an abrupt large change in the lattice orientation of the twinned region (Abdolvand, 2012; Fernández Blanco, 2014), so does detwinning. The twinned region of the crystal assumes an arrangement that represents a mirror symmetry of the remaining parent matrix with respect to the twinning plane, and undergoes reverse re-orientation during detwinning. The easily activated $(10\bar{1}2) < \bar{1}011 >$ extension twin system in Mg AZ31B alloy at room temperature (Choi et al., 2009) features a lattice reorientation angle of 86.3° (Wonsiewicz, 1966) and the characteristic shear strain of 0.129 (Fernández et al., 2013). It is readily activated under tension parallel or compression perpendicular to the c -axis (Hong et al., 2010).

Given the prominent influence of detwinning on the mechanical behaviour of such polycrystalline alloys as those of magnesium (Wang et al., 2014; Wu et al., 2008; Wu et al., 2012), it is necessary to understand and describe correctly its underlying mechanisms. Alongside intensive experimental investigation in the recent decades (Xin et al., 2014; Yin et al., 2008), simulation models are being developed for modeling the twinning-detwinning (TDT) process (Agnew et al., 2018; Hama et al.,

2017; Kabirian et al., 2015; Kondo et al., 2014; Liu et al., 2018; Paramatmuni and Kanjarla, 2018; Proust et al., 2009; Qiao et al., 2015; Wang et al., 2012; Wang et al., 2013). Most of them utilize self-consistent crystal plasticity models (Kabirian et al., 2015; Proust et al., 2009; Qiao et al., 2015; Wang et al., 2012; Wang et al., 2013) and choose to ignore the difference in the value of critical resolved shear stress (CRSS) between twinning and detwinning (Hama et al., 2017; Wang et al., 2012; Wang et al., 2013). To model the process of detwinning, rather than introducing a separate detwinning system, Proust *et al.* (Proust et al., 2009) favored the predominant twin system that had already twinned during loading by giving other twin systems in the twinned region higher CRSS values upon reloading. Even though the detwinning CRSS was practically smaller than twinning CRSS during simulation, the model failed to give a specific value for detwinning CRSS. Wang *et al.* (Wang et al., 2012; Wang et al., 2013) employed elastic viscoplastic self-consistent model to include TDT mechanisms for polycrystalline hexagonal close packed (HCP) metals. The TDT model treats a newly formed twin band (child) as a new grain and was validated against experimental data of magnesium AZ31B alloy under cyclic loading and strain path changes. Nevertheless, no additional parameters for detwinning were introduced into the model and, as a result, the CRSS values for twinning and detwinning were not separated. Based on Wang et al.'s model, Qiao et al. (Qiao et al., 2015) used the same CRSS values for twin growth and twin shrinkage (similar to partial detwinning) in an elasto-viscoplastic self-consistent model, but discriminated between the stress values needed for twin initiation (56MPa) and twin growth (32MPa) which is similar to supporting different CRSS values for twinning and detwinning. A crystal plasticity finite element model (CPFEM) was proposed to include twinning and detwinning by Hama *et al.* (Hama et al., 2017) in order to investigate the deformation response of commercial pure titanium Grade 1 sheet under various strain paths. Both $(10\bar{1}2)$ extension twin and $(11\bar{2}2)$ contraction twinning systems were considered alongside another five slip systems. $(10\bar{1}2)$ extension detwinning is set to be activated when the positive sign of resolved shear stress (RSS) is inverted to be negative. Similarly, to activate $(11\bar{2}2)$ contraction detwinning, the sign of RSS needed to be inverted from negative to positive. Again, no additional parameter was implemented for the CRSS value of detwinning. Most of the work mentioned above concentrates on developing CPFEMs to include detwinning process and correctly match experiment results.

Aside from including a complete set of deformation systems (slip, twinning and detwinning), it is also important to examine the model's capability of matching the experimental results at all structural levels of consideration. The very recent study concerned the multiscale accuracy of the simulation, but the model only included twinning not detwinning (Bong et al., 2018). Zhang *et al.* discussed the effects of microstructural grain and geometric size on plastic heterogeneities in pure copper foils on multiple levels (Zhang et al., 2018). There have also been persistent attempts made in the literature (Barnett et al., 2008; Lou et al., 2015; Shi et al., 2015) to use Schmid Factor (SF) analysis to predict local slip and twinning activity. This system of approaches is based on several assumptions. Firstly, the macroscopic (i.e., Type I) applied stress is used in the calculation of the local Resolved Shear Stress (RSS) on a given slip or twinning system. Secondly, even though account is made for the initial difference between CRSS values for different systems, the evolution of CRSS cannot be taken into account without detailed modeling based on local (i.e., Type II+III) stress and plastic strain history. In this context, the present analysis highlights the fact that correct prediction of complex deformation behavior must take into account the full Type I+II+III stress effects at specific locations within the material.

In this paper, a CPFEM is extended from a previous model to include detwinning with a set of independent parameters including its CRSS, which is calibrated against experimental results. The activation of deformation systems, particularly the onset and the end of the twinning and detwinning processes, is determined by experimental observations from *in situ* X-ray diffraction (XRD) and *in situ* EBSD during compression-tension loading. The model was then examined to represent the experimental results at all scales corresponding to Type I, Type II and Type III stresses via comparison with experiments including macroscopic loading test (Type I), XRD (Type II) and EBSD (Type III). Finally, SF analysis was performed to highlight the importance of considering all scales when it comes to investigating the deformation mechanisms.

2. Experiments

2.1. Material

The material used in this paper was commercially available wrought magnesium alloy AZ31B with average grain size at approximately 20 μ m. Typical rod texture was found in the material meaning that basal poles were mainly parallel to normal direction (ND). Therefore, twinning is preferentially activated under compression along transverse direction (TD) or rolling direction (RD) (Zhang et al., 2016), and detwinning is expected to happen upon load reversal. Dog-bone-shaped samples were machined using electrical discharge machining and their cross-section was 1mm wide and 2mm thick. The loading direction (LD) of compression-tension testing was parallel to TD in the macroscopic tests, as well as in XRD and EBSD experiments.

2.2. Macroscopic Compression-Tension Loading

The macroscopic response of the material was obtained through compression-tension test with loading rig Deben (5kN, MT10223). The loading rate was 0.2mm/min both for compression and tension. The maximum compressive engineering stress -112.7MPa (at -250N) was first reached then followed by reloading and tension until fracture at nearly 560N. Three tests were conducted to extract the average stress-strain curve with good precision.

2.3. XRD

In situ XRD experiments were conducted at Beamline B16, Diamond Light Source (Harwell Campus, UK). The monochromatic X-ray beam was set to 18keV and shaped to size 1mm \times 1mm by two sets of slits with the first set determining the size of the beam and the second set performing ‘beam cleaning’ by removing the edge scattering from the first set. The same 5kN Deben loading rig used for macroscopic test was placed in the beam for the *in situ* compression-tension test (see Figure 1(a)). The distance between the sample and the detector (Photonic Science X-ray Image Star 9000, 3056 \times 3056pixels, 31 μ m pixel size) was only roughly 130mm so that only three Debye-Scherrer rings appeared on the diffraction pattern in order to achieve a higher spatial resolution. The *in situ* compression-tension loading performed for XRD was the same as the macroscopic test except that

loading forces were kept constant after each increment of 10N for XRD pattern collection. Stress control was chosen here since the activation of twinning and detwinning is controlled by stress. Exposure time of every pattern was 200s to ensure sufficient intensity for accurate peak fitting. Analysis of the load-displacement traces confirmed that creep was negligible during 200s hold, so that the difference between stress control and strain control made little difference in this case.

2.4. EBSD for Initial Texture Measurement

For *in situ* EBSD, the dog-bone samples were polished in the sequence of 1200 grit SiC paper, 3 μm diamond suspension, 1 μm diamond suspension followed by colloidal silica. A pre-tilted grip was specially designed for Deben loading rig to satisfy the geometry where the sample surface was required to be 70° tilted, see Figure 1(b).

Informed by XRD experiments, four measurement points (B, C, E and F) were chosen for EBSD mapping. The four points chosen correspond to the stage right before twin inception, at the maximum compression force, in the middle of the detwinning process and at the end of detwinning, respectively. EBSD mapping was performed at 25kV scanning electron microscope accelerating voltage with spatial resolution of 0.8 μm . To make sure that the mapping was carried out on the same area four markers were deposited at the four corners of the rectangle area for mapping using gas injection system for Pt sputtering. Due to surface deformation resulted from deforming, when covering the same rectangle, the sizes of maps slightly vary. Similarly, the *in situ* loading process for EBSD was the same as the macroscopic test and the loading cell was kept at specific positions for mapping. Post-processing was performed using CHANNEL 5 software for the inverse pole figure coloring maps and MTEX (Nolze and Hielscher, 2016) for the pole figures. Both of them were plotted from the perspective of ND.

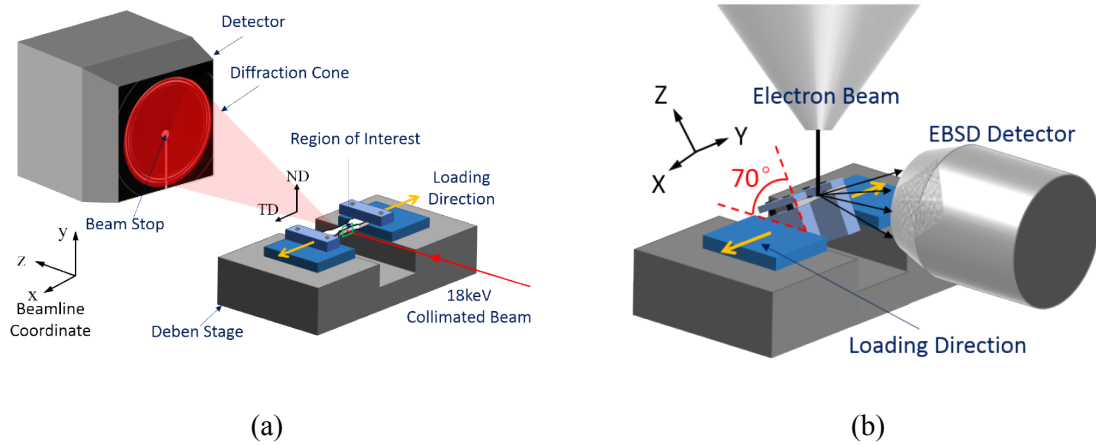


Figure 1 Experiment setup: (a) in situ XRD; (b) in situ EBSD

3. Numerical Model Setup

3.1. Finite Element Setup

Two finite element models were used in this work which were built based on the formulation reported in previous papers (Fernández et al., 2013; Fernández et al., 2011). The starting texture was imposed upon the initial grain orientation distribution in the models. Both models had 2,592 grains each characterized by specific Euler angles. The first model used in (Fernández et al., 2011) was simplified to one element per grain, which reduced calculation time by more than 90%. This approach will be referred as Model 1 in the following discussion. The second model (referred to as Model 2) was reported before (Fernández et al., 2013) and was meshed with hundreds of elements for each grain to allow carrying out the investigation of intra-granular deformation. As the details of both models can be found in the previous papers, only the more complete Model 2 is briefly described below. 3D Voronoï tessellations were generated to represent the polycrystalline aggregate. The cubic polycrystalline representative volume element (RVE) sample (see Figure 2) had a volume of 1mm^3 . A total number of 475,947 tetrahedral elements were meshed with the software package Neper (Quey et al., 2011) for polycrystal generation and meshing. The notations 'Y0' and 'Y1' were introduced for the two surfaces perpendicular to Y-axis in Figure 2. Y1 was set to have zero displacement in all directions, while Y0 has zero displacement along both X-axis and Z-axis, and a displacement in the

Y-axis was applied for the compression-tension loading. A user subroutine `vumat` in the commercial software ABAQUS/Explicit used to implement crystal plasticity constitutive law including slip and twinning was modified for the purpose of the present study to allow predicting the detwinning phenomenon.

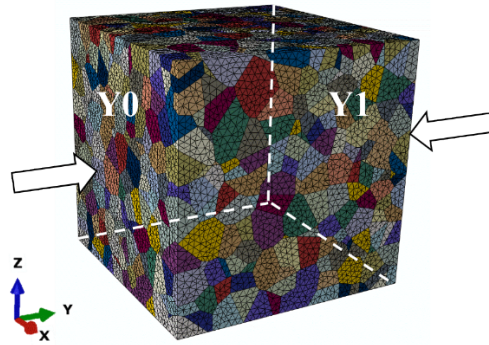


Figure 2 Cubic polycrystalline RVE used in Model 2.

3.2. Constitutive Framework

The model used in this work was extended from the CPFEM simulation developed previously by some of the authors for Mg AZ31B alloy (Fernández et al., 2013; Fernández et al., 2011) to include the contribution of detwinning to simulate the complete set of mechanisms present in the compression-tension loading process. In the following, only the detwinning constitutive behavior and its implementation in a CPFEM is presented, the reader being referred to reference papers (Fernández et al., 2013; Fernández et al., 2011) for the underlying constitutive model. Here only the $(10\bar{1}2) < \bar{1}011 >$ extension twin system and its corresponding detwin system are considered. There are six variants for twin and detwin, respectively. However, detwin variants have two sets: set 1 has exactly the same deformation plane normal and direction as its corresponding twin, while set 2 is obtained by preserving the twin plane normal, but reversing the twin direction (Table 1).

Table 1 Twinning and detwinning systems

	Twin		Detwin (set 1)		Detwin (set 2)	
	Normal	Direction	Normal	Direction	Normal	Direction
Variant 1	$(10\bar{1}2)$	$\langle \bar{1}011 \rangle$	$(10\bar{1}2)$	$\langle \bar{1}011 \rangle$	$(10\bar{1}2)$	$\langle 10\bar{1}\bar{1} \rangle$
Variant 2	$(01\bar{1}2)$	$\langle 0\bar{1}11 \rangle$	$(01\bar{1}2)$	$\langle 0\bar{1}11 \rangle$	$(01\bar{1}2)$	$\langle 01\bar{1}\bar{1} \rangle$
Variant 3	$(\bar{1}102)$	$\langle 1\bar{1}01 \rangle$	$(\bar{1}102)$	$\langle 1\bar{1}01 \rangle$	$(\bar{1}102)$	$\langle \bar{1}10\bar{1} \rangle$
Variant 4	$(\bar{1}012)$	$\langle 10\bar{1}1 \rangle$	$(\bar{1}012)$	$\langle 10\bar{1}1 \rangle$	$(\bar{1}012)$	$\langle \bar{1}01\bar{1} \rangle$
Variant 5	$(0\bar{1}12)$	$\langle 01\bar{1}1 \rangle$	$(0\bar{1}12)$	$\langle 01\bar{1}1 \rangle$	$(0\bar{1}12)$	$\langle 0\bar{1}1\bar{1} \rangle$
Variant 6	$(1\bar{1}02)$	$\langle \bar{1}101 \rangle$	$(1\bar{1}02)$	$\langle \bar{1}101 \rangle$	$(1\bar{1}02)$	$\langle 1\bar{1}0\bar{1} \rangle$

Having two sets of detwinning was needed to describe the special nature of lattice rotation in the model. In reality the lattice rotation of almost 90° takes place upon twinning under compression perpendicular to c -axis, resulting in a lattice orientation with its c -axis parallel to compression loading direction. Once the loading direction is reversed, the loading condition becomes tension parallel to the c -axis, which meets the geometry requirement and leads to detwinning. In the formulation used in the present simulation, however, lattice rotation in a twin system α only happens when the accumulative twin volume fraction f^α reaches a threshold ζ , which is a random number set to lie between 0.75 and 0.8. More details are provided in by the referenced paper (Fernández et al., 2011). As a consequence, in the simulation twinning deformation occurs and the associated shear strain begins to accumulate long before the finite element lattice rotation happens. It is possible that the external compression loading is ended after twinning starts but before lattice rotation is triggered in the model, which leads to a situation where an element has already experienced some twinning shear strain, but remains in the almost same orientation as the starting one (subtle orientation change caused by slip is not considered here). In this case, detwinning cannot be activated by reversed loading if set 1 is used for detwin variants. In order to allow detwinning, set 2 is assigned to detwin variants. Making detwin direction negative has the same effect as rotating lattice during twinning when it comes to satisfying the twinning/detwinning geometry. For simplification, the superscript i (and j) will refer to a slip

system, α (and β) to a twin system, m (and n) to a detwin system (set 1) and k (and l) to a detwin system (set 2).

To track the lattice rotation caused by twinning/detwinning, *twincounter* variable was introduced in the model. This variable is increased by 1 every time rotation happens and rotation is triggered under two conditions stated in Equation (1). At the start of the simulation, *twincounter* is set to 0 for all the elements. If the f^α of a twin system α of one element reaches the threshold ζ , twinning-induced rotation occurs (*condition1*) and *twincounter* is incremented to 1. During reverse loading, rotation from detwinning (set 1) is triggered when the detwin fraction f^m reaches the threshold and *twincounter* is increased from 1 to 2.

$$\begin{cases} \text{condition 1: } twincounter = 0 \text{ and } f^\alpha \geq \zeta, \text{ rotation due to } \mathbf{twinning} \\ \text{condition 2: } twincounter = 1 \text{ and } f^m \geq \zeta, \text{ rotation due to } \mathbf{detwinning (set 1)} \end{cases} \quad (1)$$

Let γ denote the shear strain of the system. Using $s_{\alpha/m/k}$ to denote the CRSS of twinning/detwinning systems and $\tau_{\alpha/m/k}$, the corresponding RSS, the condition for twinning/detwinning to occur is given below:

$$\begin{cases} \tau_\alpha - s_\alpha > 0, twincounter = 0: \mathbf{twinning} \\ \tau_m - s_m > 0, \gamma^\alpha - \gamma^m \geq 0.15\gamma^\alpha, twincounter = 1: \mathbf{detwinning (set1)} \\ \tau_k - s_k > 0, \gamma^\alpha - \gamma^k \geq 0.15\gamma^\alpha, twincounter = 0: \mathbf{detwinning (set2)} \end{cases} \quad (2)$$

The value of 0.15 was chosen because it has been observed **in our experiment** that only approximately 85% of twins are able to detwin (i.e., 15% of twins persist after full reverse loading). This is modeled here by retaining 0.15 of a twin's maximum shear strain during detwinning, see Equation (2). The algorithm is presented in Figure 3. In the following discussion, the difference in accumulative shear strain between twin and detwin is **called the residual twin strain**. Therefore, the residual twin **strain** that persists on the completion of load reversal accounts for 15% of the maximum twin shear strain.

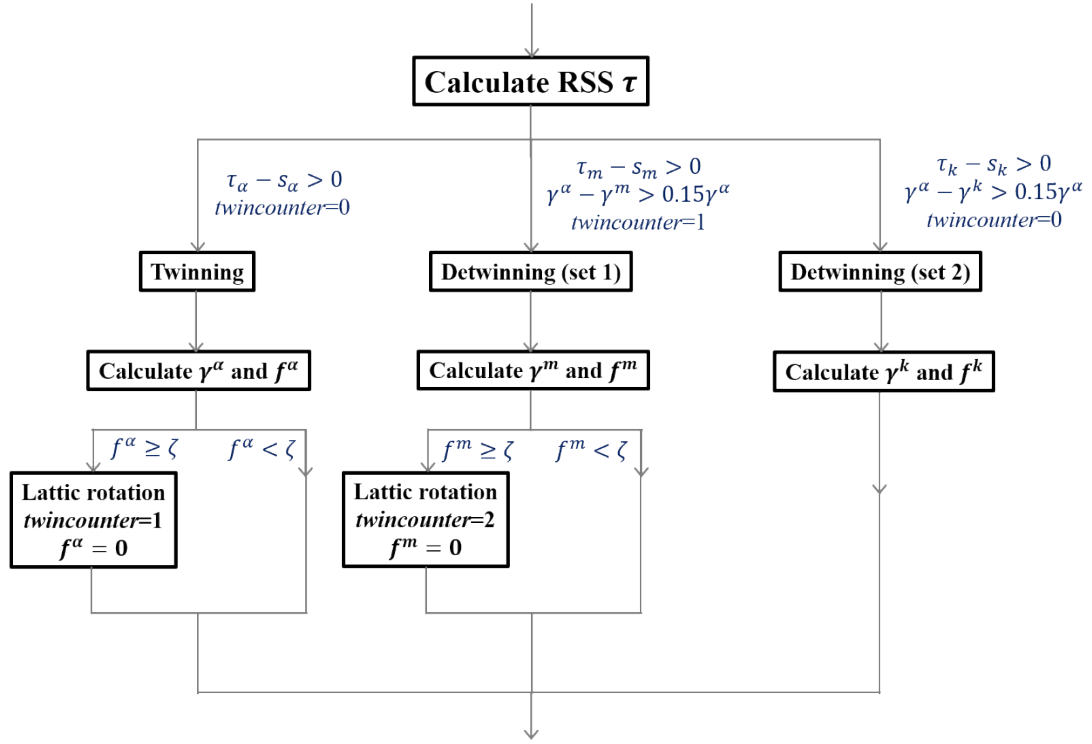


Figure 3 Flow chart of part of the algorithm concerning TDT activation and rotation.

3.3. Model Calibration

The two FE models introduced in Section 1 give almost the same macroscopic response when using identical parameters (Fernández et al., 2013). This is an important result that reflects the fact that capturing the correct shear strain in the simpler lighter model (Model 1) is sufficient to simulate the overall deformation behavior of the material in agreement with previous findings (Fernández et al., 2013). The distinction at the microscopic scale persists, nevertheless, and therefore Model 2 calibration was pursued further to ensure that micro-scale deformation phenomena are captured correctly. To improve computational efficiency, the stress-strain (thus macroscopic in nature) calibration carried out in the present study for Model 2 was started by using Model 1, the parameters of which were passed onto Model 2 for further study. The non-detwinning material parameters were taken from the literature (Abdolvand et al., 2015; Fernández et al., 2013; Fernández et al., 2011) while the detwinning parameters were calibrated so as to match the stress-strain curve, see Table 2.

Following the notation of Ref. (Fernández et al., 2011), $s_{0;basal}$, $s_{0;prism}$, $s_{0;pyr< a >}$, $s_{0;pyr< c+a >}$, $s_{0;tw}$ and $s_{0;detw}$ are the CRSS for basal slip, prismatic slip, pyramidal $<a>$ slip, pyramidal $<c+a>$ slip, twin and

detwin respectively. $h_{0;sl}$, $h_{0;tw/detw}$, $h_{0;sl-tw/detw}$, $h_{0;tw/detw-sl}$, a_{sl} , $a_{tw/detw}$, $a_{sl-tw/detw}$ and $a_{tw/detw-sl}$ are the reference hardening parameters and hardening exponents for slip-slip, twin-twin, detwin-detwin, slip-twin, slip-detwin, twin-slip, and detwin-slip interactions. Parameters s with *tilde* (\tilde{s}_{basal} , \tilde{s}_{prism} , $\tilde{s}_{pyr<a>}$, $\tilde{s}_{pyr<c+a>}$, \tilde{s}_{tw} and \tilde{s}_{detw}) are the saturation stresses for deformation systems, meaning the maximum value for the CRSS of deformation systems during hardening. q_{sl} , q_{tw} and q_{detw} are the ratios of the reference cross-hardening parameter to the reference self-hardening parameter of slip, twin and detwin systems, respectively. γ_0 is the shear strain of twin and detwin. C_{11} , C_{12} , C_{13} , C_{33} and C_{55} are the crystal stiffness elastic constants for Mg AZ31B.

Table 2. Parameters for crystal plasticity model

$s_{0;basal}$	$s_{0;prism}$	$s_{0;pyr<a>}$	$s_{0;pyr<c+a>}$	$s_{0;tw}$	$s_{0;detw}$
12.0 MPa	60.0 MPa	100.0 MPa	100.0 MPa	46.5 MPa	23.0 MPa
$h_{0;sl}$	$h_{0;tw/detw}$	$h_{0;sl-tw/detw}$	$h_{0;tw/detw-sl}$	q_{sl}	$q_{tw/detw}$
600.0 MPa	1000.0 MPa	0.0 MPa	600.0 MPa	2	1
a_{sl}	$a_{tw/detw}$	$a_{sl-tw/detw}$	$a_{tw/detw-sl}$	\tilde{s}_{tw}	\tilde{s}_{detw}
0.6	2	n/a	2	100.0 MPa	300.0 MPa
\tilde{s}_{basal}	\tilde{s}_{prism}	$\tilde{s}_{pyr<a>}$	$\tilde{s}_{pyr<c+a>}$	$\tilde{s}_{sl-tw/detw}$	$\tilde{s}_{tw/detw-sl}$
15.0 MPa	150.0 MPa	190.0 MPa	190.0 MPa	n/a	100.0 MPa
$\gamma_{0,tw/detw}$	C_{11}	C_{12}	C_{13}	C_{33}	C_{55}
0.129	58.0 GPa	25.0 GPa	20.8 GPa	61.2 GPa	16.6 GPa

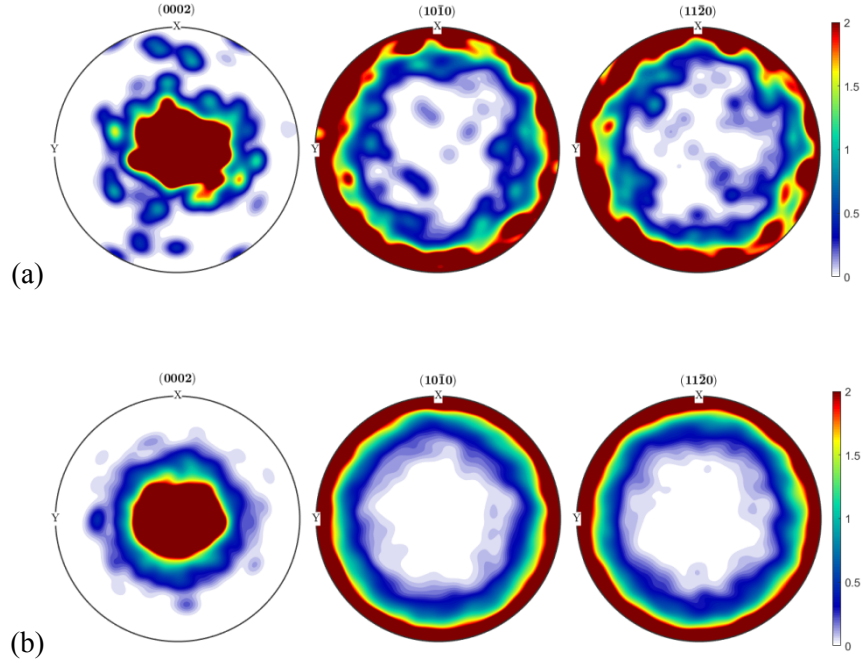


Figure 4 Initial texture of material in: (a) experiment; (b) simulation

The Euler angles for the simulation were generated by randomly distributing basal poles within 20° (distributing angle) around the north pole, so as to fit the experimental pole figures, as illustrated in Figure 4. It was verified that changing the distributing angle by $\pm 20\%$ had negligible effect on the stress-strain curves of the simulations.

4. Results

Stresses can be classified into three types based on the scale at which they are considered: Type I, Type II and Type III (Everaerts et al., 2018; Salvati and Korsunsky, 2017). Type I stresses exist at the macroscopic scale and is traditionally the main concern of design engineers, since the vast majority of the existing predictive models of fatigue crack initiation and propagation are based on Type I stress calculations. Type II and type III are both of microscopic nature, but are distinguished in terms of the scale of averaging: Type II is referred to as inter-granular and represents grain-scale average values (or, more precisely, the deviation of the grain-average stress values from the macroscopic Type I average), whilst Type III intra-granular stresses are calculated locally by averaging over nano-scale volumes (more precisely, the deviation of the local stress values from the Type I+II sum). In simple

words, Type II stresses vary between different grains, while Type III stresses vary within a grain. The total stress is the sum of the stresses of all three types.

The multi-scale stress approach to describing the stress relies on selective averaging, and can be briefly expressed mathematically as follows:

$$\begin{aligned}\sigma^{total} &= \sigma^I + \sigma^{II} + \sigma^{III}, \\ \sigma^I &= \langle \sigma^{total} \rangle_{macro}, \\ \sigma^I + \sigma^{II} &= \langle \sigma^{total} \rangle_{micro}.\end{aligned}\tag{3}$$

Averaging at different scales is performed as follows: macroscale averaging smooths out the micro- and nano-scale variation. Microscale averaging smooths out the nanoscale ‘ripple’, and produces the sum of Type I and II stresses. The total stress is the sum of Types I, II and III. This approach to total stress decomposition is based on historical convention which at present appears to be highly relevant and appropriate, and so is followed in the present study. We note that the additive nature of this decomposition means that the calculation of total stress requires the addition of Type I, II and III terms.

The results and discussion presented below concern not only the multiple scales of stress corresponding to Type I, Type II and Type III, but also the corresponding analysis of scale-dependent deformation processes.

4.1. Type I: Macroscopic Response

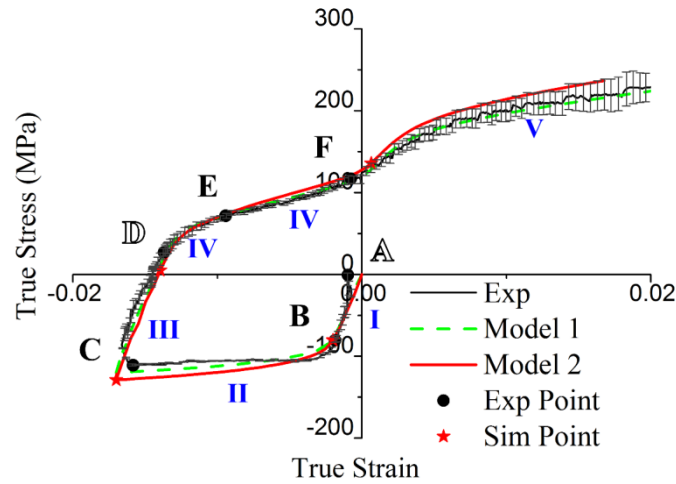


Figure 5 Comparison of the stress-strain curves from experiment and simulation. Solid dots B, C, D and F: the beginning and the end of twinning and detwinning processes, observed in the XRD and the EBSD experiments. Solid dot A: beginning of the loading; solid dot E: the intermediate stage of detwinning. Red stars: the beginning and the end of twinning and detwinning predicted by the simulation. (Note that points A and D are indicated by empty letters, because no EBSD maps were taken at these positions).

Figure 5 illustrates the macroscopic true stress vs. true strain curves obtained via experiment (with standard deviation values shown as error bars), and simulation. The six black dots correspond to the points A-F in the XRD and the EBSD experiments with B, C, D and F indicating the activation of twinning/detwinning, whereas the four red stars mark the beginning and the end of twinning and detwinning as predicted by the simulation. EBSD maps were not taken at black dots A and D, which is indicated by making the letters hollow in Figure 5. The start and the end of twinning are well matched in the simulation and experiment, whereas detwinning occurs over a somewhat longer range of strain in the simulation. To understand more fully the effect of deformation systems on the macroscopic curve, it is worth comparing these results with Figure 5(c). It is obvious that the flat area II during compression mainly results from twinning. For reverse loading, the first 'dip' lies at IV and is caused by detwinning. The second jump that appears at V is the consequence of the prismatic slip kicking in. It can be concluded that the CPFEE model captures correctly the macroscopic stress-strain curve and it is capable to predict Type I behavior.

The earlier calibration of the CRSS values for twin and detwin led to 46.5 MPa and 23.0 MPa, respectively. It has already been reported that detwinning is likely to happen at lower CRSS compared

to twinning (Qiao et al., 2015). One reason for this is that no nucleation is required during detwinning. The second reason that is worth mentioning is that the backstress introduced by twinning is likely to act to promote the reverse process of detwinning. 56 MPa and 32 MPa have been reported to be the CRSS values needed for twin initiation and twin growth, respectively (Qiao et al., 2015). Even though the absolute values vary slightly, the difference between twinning CRSS and detwinning CRSS is almost the same, being 23.5MPa in our paper and 24 MPa in the other report.

4.2. Type II: Activation of Twinning and Detwinning

XRD investigates the average behavior of an aggregate of grains while EBSD is able to show individual grains in a micro-scale area. Therefore, by comparing the simulation results against the experimental data (both XRD and EBSD), the capability of the model in representing Type II can be discussed. Figure 6 illustrates the comparison between the simulation and the experiment. Fit2D software was employed for analyzing the XRD patterns. Radial binning with azimuthal integration (caking angle 30°) (Zhang et al., 2016) was performed in a way such that the $1_{-}(100)$ plot represents a group of grains with their $(10\bar{1}0)$ plane normal parallel to the TD (as well as LD). The same rule applies to the $2_{-}(002)$ and $3_{-}(101)$ curves, meaning that they respectively indicate groups of grains with their (0002) plane and $(10\bar{1}0)$ plane parallel to the TD. It is considered here that the intensity value corresponds to the volume of grains that are contributing to the Debye-Scherrer diffraction ring (Qiao et al., 2015). It can be observed in Figure 6(b) that an abrupt change in intensity corresponding to the rotation of grains starts from point B. Over the loading period between points B and C, a large amount of grains initially with their $(10\bar{1}0)$ plane normal parallel to the TD direction experience a rotation of nearly 90° , leaving their (0002) plane normal parallel to the TD. A reverse rotation is indicated from point D to F under reverse loading. Combined with EBSD maps, it can be confirmed that the rotation observed in the B-C and D-F loading periods is caused by twinning and detwinning, respectively. A more visual illustration of the rotation described is given by the insets showing HCP unit cell orientation in Figures 6(b) and (d).

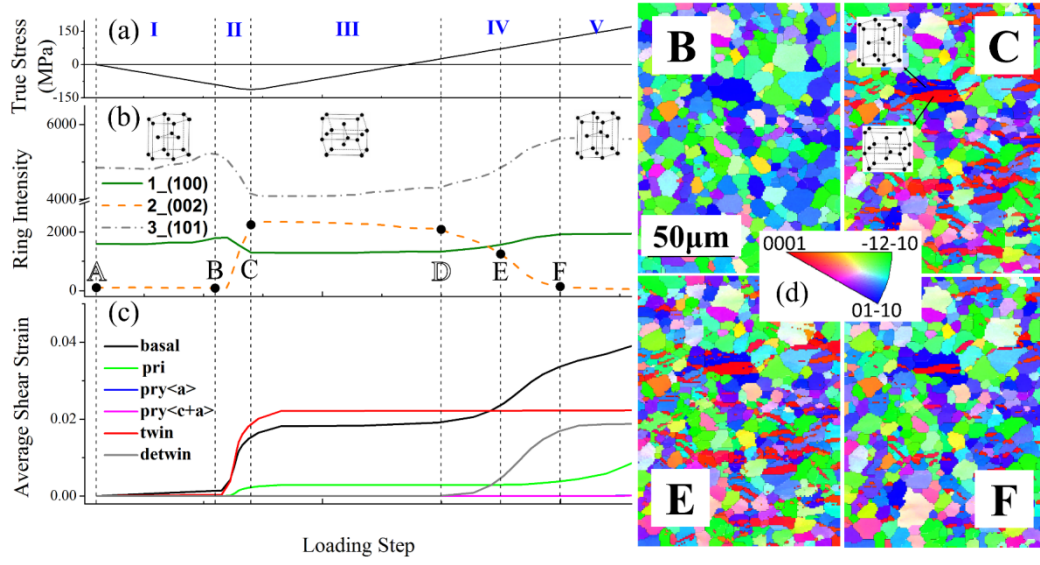


Figure 6 Change of quantities with loading step: (a) macroscopic true stress; (b) intensity of the first three Debye-Scherrer rings in XRD experiment; (c) average shear strain of individual deformation systems in simulation; (d) in situ EBSD maps of measurement point B, C, E and F

The average shear strain of deformation systems in Figure 6(c) is the mean value of accumulative shear strain of all the twinned elements at one loading step as predicted by the simulations and making use of the Matlab post-processing package Abaqus2Matlab (Papazafeiropoulos et al., 2017).

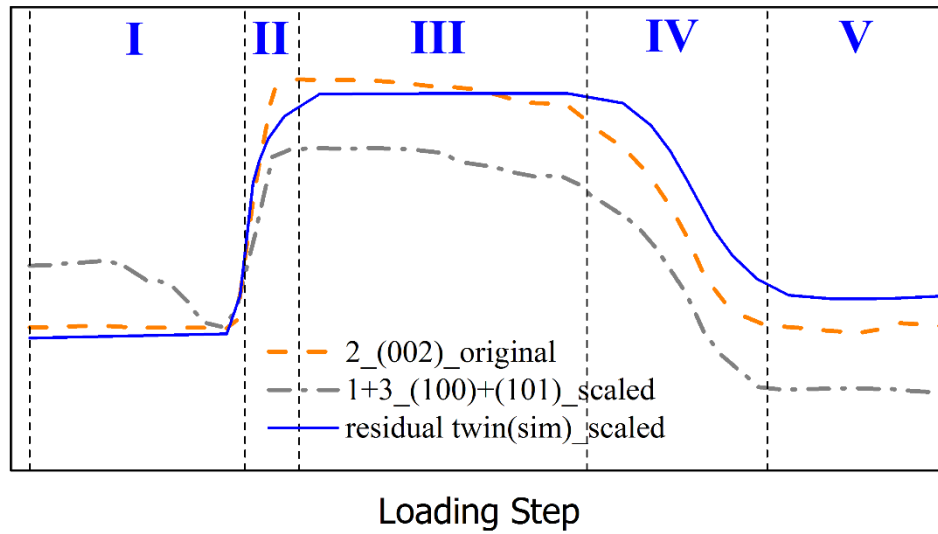


Figure 7 Superposition of intensity plot of 2_(002) (original), sum 1_(100) and 3_(101) (scaled) from XRD and residual twin shear strain (scaled) from simulation

In order to further examine the activation of twinning and detwinning predicted by simulation and experiment, Figure 7 shows the superposition of several plots. The dashed orange line is the original intensity plot of the 2nd ring which is the same as the dashed orange line in Figure 6(b). The grey dashed-dotted line is the sum of intensity of the 1st ring and the 3rd ring which was flipped and shifted so that it can be compared to the 2₍₀₀₂₎ plot. The residual twin shear strain in the simulation represented by solid blue line is the difference between the accumulative shear strain of twin and detwin. It was scaled to match the intensity magnitude from XRD. Note that the dashed lines are the measured intensity values for specific peak Miller indices that reflect the reorientation of the lattice caused by twinning and detwinning related to specific diffraction planes, while the solid line is the simulated average shear strain of twinning over all grains. These two quantities should not be confused, but are shown here together for the purpose of examining the start and end of twinning and detwinning. It is evident that the orange dashed line and the blue solid line almost overlap, especially at the stage of twinning. This illustrates that the simulation gives a reliable prediction of the onset and completion of twinning and detwinning.

The simulation outcome demonstrates a good match with both of the experiments in terms of the activity of deformation systems. Therefore, it can be concluded that the model can achieve a satisfying degree of accuracy and reliability when it comes to inter-granular scale corresponding to Type II stresses. Additionally, it can be seen that basal slip and twinning are the most active deformation systems from point B to C, followed by detwinning from D to F. After detwinning is no longer available, prismatic slip begins, which is in agreement with the conclusion of the previous study (Agnew et al., 2003).

4.3. Type III: Morphology of Twinning

To discuss the model's capability to capture the deformation at the intra-granular scale, it is first necessary to examine whether the model is able to present the morphology of individual twins correctly. Figure 8 shows the contour plot of the difference in accumulative shear strain between twinning and detwinning (the difference here is essentially residual twin shear strain) at different true strain values. Figure 8(I) and (II) depict the RVE as a 3D volume. Figure 8(a)-(i) show the cross-

section at the middle of the material RVE indicated by the red plane in **Figure 8(II)**. The amount of twinning is increasing from Figure 8(a) to (d) under compressive loading. Following that, under increasing tension, detwinning begins to happen and the amount of twinned regions decreases. The amount of twinning reaches its maximum at the end of compression in Figure 8(e). It is evident that there are several grains in the central area in Figure 8(e) which have little twinning unlike their surrounding grains. Additionally, intra-granular variation in shear strain and strain localization at the grain boundaries exists, as pointed out by red arrows in Figure 8(e). These effects might arise from the discontinuousness of deformation between the grain and its neighbors: local concentration level increases when the surrounding grains do not have suitable systems to accommodate the sudden change brought by twinning/detwinning in the grain.

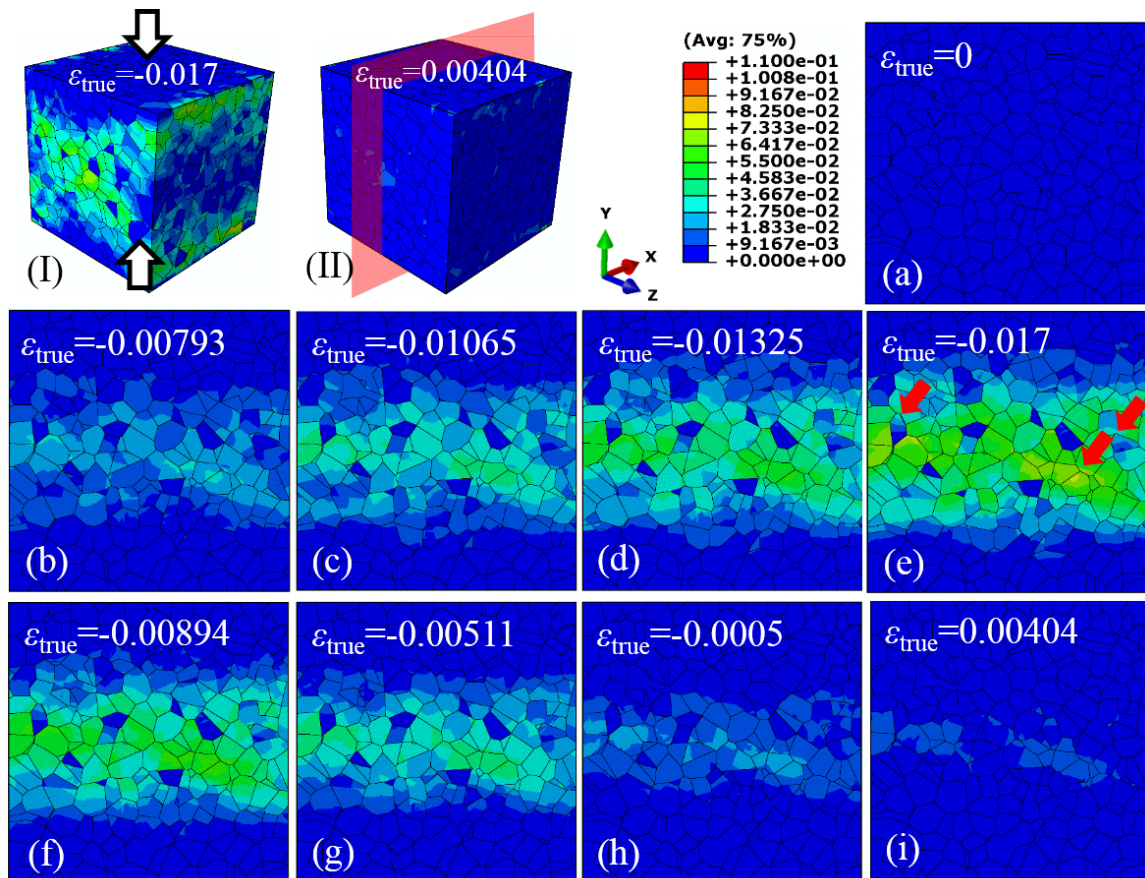


Figure 8 Contour plot of amount of residual twin shear strain at different true strain values (refer to colour bar for levels): (I) and (II) the RVE as a 3D volume; (a)-(i) the cross-sections at the middle of the RVE indicated by the red plane in (II).

The current model, however, is not able to represent correctly the morphology of twins shown in the EBSD maps in Figure 6(d). This indicates that further refinements potentially involving non-local effects or finer meshes as proposed previously by Fernandez *et al.* (Fernández et al., 2013) are required in order to capture the details of the intra-granular behavior and local grain interaction. Nevertheless, the model allows the investigation of the effect of statistical distribution of Type III stresses at the inter-granular level as discussed below.

4.4. Multi-Scale Representation

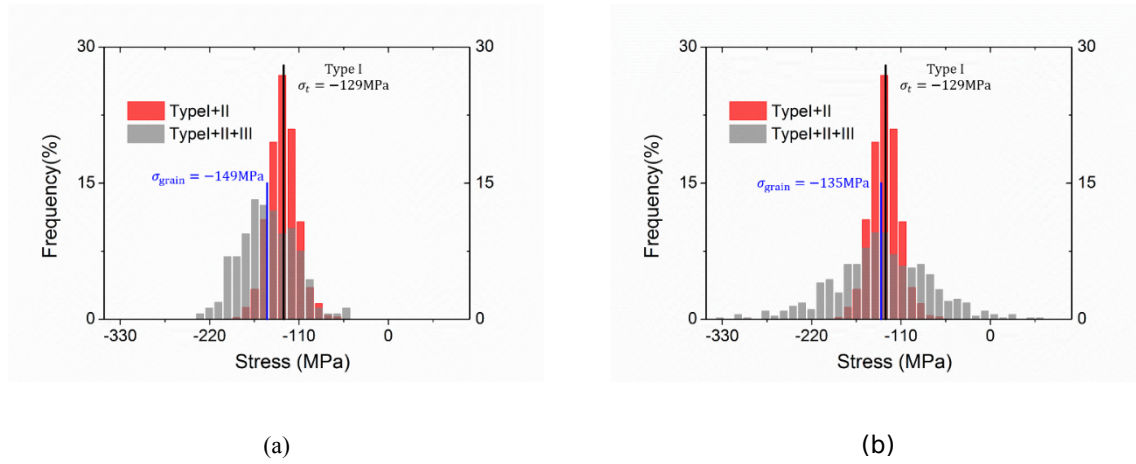


Figure 9 Comparison between three types of stresses represented by the simulation: (a) grain 1 for Type I+II+III analysis; (b) grain 2 for Type I+II+III analysis.

In order to allow the analysis of multi-scale stress state within the material, we consider the statistical distribution of stresses obtained by averaging at different scales.

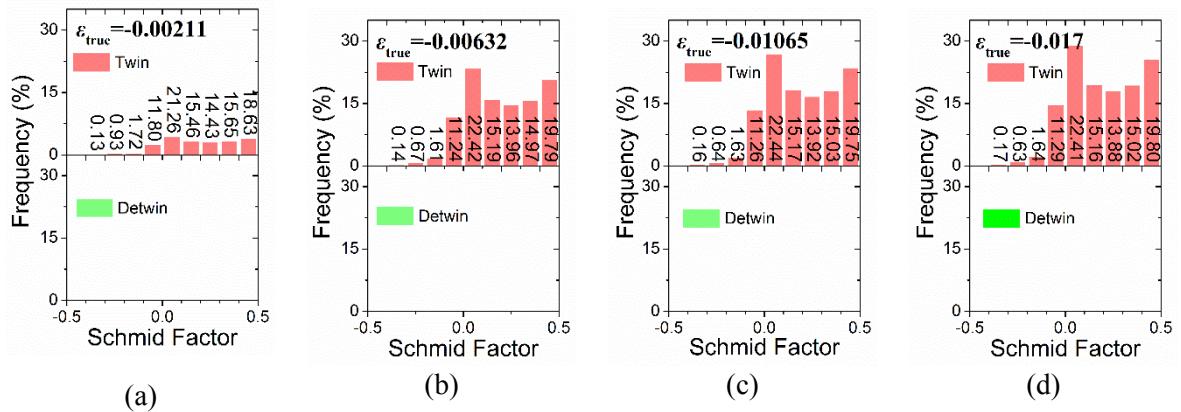
Figure 9 shows a histogram representation of the stresses obtained at the end of the compressive loading stage (point C in Figure 5), comparing three types of stresses extracted from Model 2. The vertical black line represents the value (-129 MPa) of the macroscopic true stress in the loading direction. The red columns illustrate the statistical distribution of stress values (Type I+II) along the loading direction obtained by averaging over all elements belonging to each grain. It is clear that the average of S22 Type I+II stresses corresponds to Type I macroscopic stress, but the distribution has fairly large Gaussian width of ~20 MPa.

Finally, the grey columns in Figure 9(a) and 9(b) represent the histograms of the total “pointwise” (local, element level) Type I+II+III stresses for two arbitrary grains (grain 1 and grain 2). It is apparent here that the width of the statistical distribution of Type I+II+III stresses is found to be greater than that of Type I+II stresses, reflecting the greater degree of oscillation of stress at the nano-scale. Figure 9(a) is related to a grain 1 that had the average Type I+II stress value of -149 MPa, whilst Figure 9(b) refers to grain 2 that had Type I+II stress value of -135 MPa.

It is apparent that the width of the statistical distribution of Type I+II+III stress values in grain 2 (Figure 9(b)) is much wider than that for grain 1 (Figure 9(a)), and is in fact comparable in magnitude with the macroscopic Type I average. This leads to some points experiencing tension under overall compression of the RVE, whilst some other points have over double the absolute value of the average macroscopic applied compressive stress. This situation arises due to the large amount of plastic deformation involving slip and twinning/detwinning in this grain. The implications of these findings are analysed in the Discussion (section 5) below.

To highlight the importance of taking these effects into consideration, the analysis below shows that the use of ‘classical’ SF analysis does not lead to good agreement with the model predictions.

4.5. Statistics of Schmid Factors



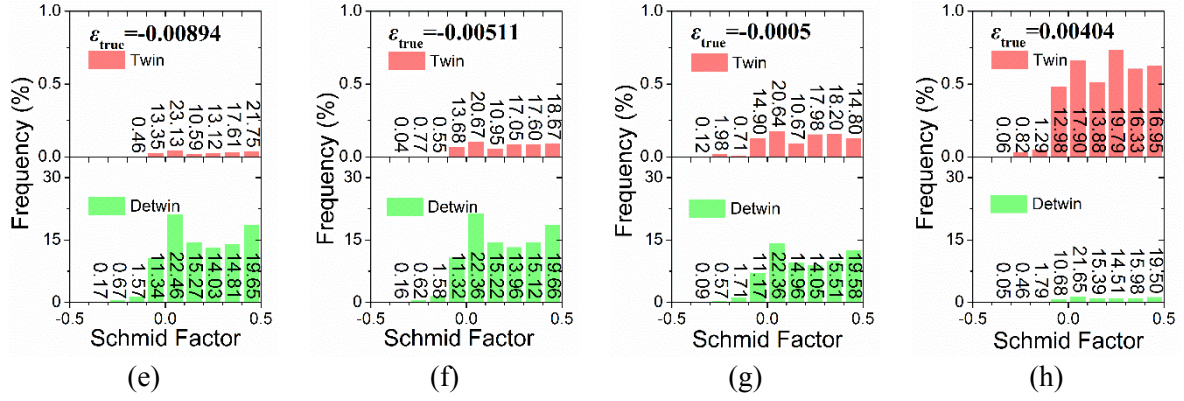


Figure 10 Statistics of SFs at different strain levels: ratio of the number of active twinning/detwinning variants to the total number of elements in the RVE and relative proportions (note that the range of vertical axes is the same except for the top limit in (e)-(h))

In this section, the SF statistics is considered based on the calculation using the applied macroscopic stress and the current grain orientation. In this sense, the ‘localization’ of stress (i.e., the difference between the applied stress, Type I, and the local stress value due to Type II+III effect) is ignored, but the grain rotation acquired due to plastic deformation history (twinning and slip) is taken into account.

Figure 10 shows the statistics of SFs values at various strain levels in the form of a histogram. Figure 10(a)-(d) correspond to compression, and (e)-(h) to tension. The calculation of SFs was based on individual elements and only elements with $\dot{\gamma} > 0$ in the current simulation increment were included in the statistics, meaning that all elements were undergoing twinning or detwinning at that increment. There are two percentage values shown for each plot: one is the vertical axis ‘Frequency (%)’ which is the ratio of the number of active twinning/detwinning variants to the total number of elements in the RVE (475,947). The numbers on each column represents the relative frequency (i.e., the ratio of the number of active twinning/detwinning variants within the specific SF range to the total number of active twinning/detwinning variants at the current strain level).

The ‘classical’ SF analysis expects that most activated twinning or detwinning variants should have relatively high values of SF (Jonas et al., 2011). However, Figure 10 shows a fairly even distribution of SFs with a slightly larger percentage for small SFs for both twinning and detwinning. The local variation in stresses increases with the rise of external loading. When the local variation or

concentration is large, it is the micro- and nano-scale stresses that are more dominant in terms of deciding whether twinning / detwinning is activated or not.

4.6. Lattice Rotation

The simulation using Model 1 did not exhibit any element lattice rotation. As a comparison, the same starting texture was used for the simulation of Model 2 and rotation was triggered in a small volume of elements. This is due to the binary nature of the element lattice rotation characteristic of the formulation of this constitutive model (Fernández et al., 2011). The compression loading in the current simulation did not reach the threshold strain levels leading to the model lattice rotation. It was also discussed that Model 2 has results in a smaller delay compared to Model 1. This is mainly because the more detailed model allows inter-granular variation which leads to local strain concentration in turn causing lattice rotation (Fernández et al., 2013).

In spite of the fact the actual rotation of the elements is delayed with respect to the experimentally observed lattice rotation, the macroscopic behavior of the material is adequately captured. As already discussed in previous work (Fernández et al., 2013), this apparent discrepancy can be rationalized by the fact that rotation is a micro-scale localized phenomenon at the onset, and its influence on the activation of deformation systems is then insignificant. The model thus assumes that the element rotation is only needed when the lattice twin rotation is starting to alter the lattice plasticity at the grain level. Overall, the prediction of the macroscopic behavior by the model was observed to be trustworthy (Fernández et al., 2013). We thus follow here the same approach for the detwinning rotation, while accounting for the detwinning occurring in the absence of element lattice rotation. It is worth mentioning that the CRSS is considered to be the property of the deformation system itself, unchanged by the orientation of the grain and its neighboring grains. Therefore, CRSS values mentioned above should not be affected by rotation.

5. Discussion

The results presented above represent an implementation of the hierarchical multi-scale approach to the analysis of stresses within plastically deformed polycrystal aggregates. The systematic

evaluation and assessment of individual stress contributions (Type I, II and III) has been carried out using statistical distributions. It was found that the spread of stress values around the macroscopic average increases as the consideration progresses towards finer scales. The Type I+II stress sum varies from grain to grain, meaning that the local conditions for the onset and continuation of plastic deformation cannot be predicted entirely based on the macroscopic applied stress and initial grain orientation and CRSS using the 'classical' SF approach. Instead, full multi-scale simulation is required. Furthermore, at the intra-granular level of consideration (Type I+II+III), even wider distribution of stress values is observed, attesting to the inhomogeneity of deformation and load sharing within individual grains. It is precisely this inhomogeneity that is responsible for the emergence of the twinning patterns obtained from EBSD analysis shown in Figure 6(d).

It is concluded that a rational requirement for a validated multi-scale model is to match the macroscopic stress-strain curve of the material, but also, importantly, the statistics of stress distributions at the inter-granular (Type II) and intra-granular (Type III) levels, along with the grain rotation (texture change) effects that can be validated against such techniques as XRD analysis.

6. Conclusion

In this study, **three types of experiments** were carried out on the commercial magnesium alloys AZ31B: macroscopic compression-tension test, *in situ* XRD and *in situ* EBSD, in order to investigate the activation of different plastic deformation systems during mechanical loading at all scales. In the *in situ* synchrotron XRD experiment, the change of intensity of the Debye-Scherrer rings for different grain groups was considered as an indication of the volume fraction of twinning and detwinning. This was verified in a spatially resolved fashion by *in situ* EBSD through direct observation of crystal rotation induced by twinning and detwinning. A crystal plasticity model was developed to account for the activity of four slip systems, twinning and particularly detwinning with a set of independent parameters allowing the calibration of its CRSS value. The model was utilised with finite element models with largely different calculation sizes: one grain has only one element in the Model 1 and multiple elements in the Model 2. It was known that the parameters calibrated for the Model 1 can be

shared to the Model 2 without much change in the stress-strain curve. The information on deformation system activity gathered from experiments was essential for calibrating the parameters for the models. It was used to determine the CRSS of detwinning (23 MPa), which was found to be significantly lower compared to the CRSS of 46.5 MPa for twinning. The capability of the models in representing the experiments is examined on multiple scales corresponding to Type I, Type II and Type III stresses. On a macroscopic level with respect to Type I, the calibrated models were capable of correctly predicting the macroscopic stress-strain curve. For Type II which is on a micro-scale, the beginning and end of plastic deformation systems is satisfyingly predicted by the model validating the model's competency in investigating Type II matter. Through comparison of twin morphology between EBSD maps and shear strain contour maps from the simulation, it was concluded that the current model is not able to represent the real morphology of twins. This is an important requirement if the model is to be used to study Type III stresses. However, it is apparent that this would require introducing non-local effects into the description, and also significantly refining the mesh around the twins. For the purposes of the present analysis, it is more meaningful to use the model for statistical analysis. Evaluation of the entire model shows that the nano-scale stresses display a higher degree of oscillation than stresses at the micro-scale. The statistics of SFs further proves the importance of considering the effects of Type II and Type III stresses. Lastly, the examination of lattice rotation in the model concluded that even though only a small amount of crystal rotation was observed in the simulation, the macroscopic behavior shown by the CPFEE model was weakly affected by micro-scale rotation, and provided a reliable match to the observations.

7. Acknowledgement

The authors are grateful to Beamline B16 (Diamond Light Source, Harwell Campus, UK) for the support and help with the X-ray diffraction experiment, and the provision of beamtime under allocation MT15184-1. The experimental work was partially supported by the laboratory for In-situ Microscopy and Analysis (LIMA) and Multi-Beam Laboratory for Engineering Microscopy (MBLEM) in Department of Engineering Science, University of Oxford. Support is acknowledged from EPSRC (EP/P005381/1), and the Research Complex at Harwell, under the Centre for In situ

Reference

- Abdolvand, H., 2012. Multi-scale modeling and experimental study of deformation twinning in hexagonal close-packed materials. Queen's University, Kingston, Ontario, Canada.
- Abdolvand, H., Majkut, M., Oddershede, J., Schmidt, S., Lienert, U., Diak, B.J., Withers, P.J., Daymond, M.R., 2015. On the deformation twinning of Mg AZ31B: A three-dimensional synchrotron X-ray diffraction experiment and crystal plasticity finite element model. *International Journal of Plasticity* 70, 77-97.
- Agnew, S., Tomé, C., Brown, D., Holden, T., Vogel, S., 2003. Study of slip mechanisms in a magnesium alloy by neutron diffraction and modeling. *Scripta Materialia* 48, 1003-1008.
- Agnew, S.R., Singh, A., Calhoun, C.A., Mulay, R.P., Bhattacharyya, J.J., Somekawa, H., Mukai, T., Clausen, B., Wu, P.D., 2018. In-situ neutron diffraction of a quasicrystal-containing Mg alloy interpreted using a new polycrystal plasticity model of hardening due to {10.2} tensile twinning. *International Journal of Plasticity* 100, 34-51.
- Avedesian, M.M., Baker, H., 1999. ASM speciality handbook: magnesium and magnesium alloys. ASM International, Novelty, Ohio, USA.
- Barnett, M.R., Keshavarz, Z., Beer, A.G., Ma, X., 2008. Non-Schmid behaviour during secondary twinning in a polycrystalline magnesium alloy. *Acta Materialia* 56, 5-15.
- Bong, H.J., Hu, X., Sun, X., Ren, Y., 2018. Mechanism-based constitutive modeling of ZEK100 magnesium alloy with crystal plasticity and in-situ HEXRD experiment. *International Journal of Plasticity*.
- Choi, S.H., Kim, D.H., Lee, H.W., Seong, B.S., Piao, K., Wagoner, R., 2009. Evolution of the deformation texture and yield locus shape in an AZ31 Mg alloy sheet under uniaxial loading. *Materials Science and Engineering: A* 526, 38-49.
- Cui, Y., Li, Y., Wang, Z., Lei, Q., Koizumi, Y., Chiba, A., 2017. Regulating twin boundary mobility by annealing in magnesium and its alloys. *International Journal of Plasticity* 99, 1-18.
- Everaerts, J., Salvati, E., Uzun, F., Romano Brandt, L., Zhang, H., Korsunsky, A.M., 2018. Separating macro- (Type I) and micro- (Type II+III) residual stresses by ring-core FIB-DIC milling and eigenstrain modelling of a plastically bent titanium alloy bar. *Acta Materialia* 156, 43-51.
- Fernández, A., Jérusalem, A., Gutiérrez-Urrutia, I., Pérez-Prado, M., 2013. Three-dimensional investigation of grain boundary-twin interactions in a Mg AZ31 alloy by electron backscatter diffraction and continuum modeling. *Acta Materialia* 61, 7679-7692.
- Fernández, A., Prado, M.T.P., Wei, Y., Jérusalem, A., 2011. Continuum modeling of the response of a Mg alloy AZ31 rolled sheet during uniaxial deformation. *International Journal of Plasticity* 27, 1739-1757.
- Fernández Blanco, A.M., 2014. Continuum models of the mechanical behavior of rolled and die-cast magnesium alloys. Escuela Técnica Superior de Ingeniería Informática, Universidad Politécnica de Madrid, Málaga, Spain.
- Groves, G., Kelly, A., 1963. Independent slip systems in crystals. *Philosophical Magazine* 8, 877-887.
- Hama, T., Kobuki, A., Takuda, H., 2017. Crystal-plasticity finite-element analysis of anisotropic deformation behavior in a commercially pure titanium Grade 1 sheet. *International Journal of Plasticity* 91, 77-108.
- Hong, S.-G., Park, S.H., Lee, C.S., 2010. Role of {10-12} twinning characteristics in the deformation behavior of a polycrystalline magnesium alloy. *Acta Materialia* 58, 5873-5885.

- Jonas, J.J., Mu, S., Al-Samman, T., Gottstein, G., Jiang, L., Martin, É., 2011. The role of strain accommodation during the variant selection of primary twins in magnesium. *Acta Materialia* 59, 2046-2056.
- Kabirian, F., Khan, A.S., Gnäupel-Herold, T., 2015. Visco-plastic modeling of mechanical responses and texture evolution in extruded AZ31 magnesium alloy for various loading conditions. *International Journal of Plasticity* 68, 1-20.
- Khan, A.S., Pandey, A., Gnäupel-Herold, T., Mishra, R.K., 2011. Mechanical response and texture evolution of AZ31 alloy at large strains for different strain rates and temperatures. *International Journal of Plasticity* 27, 688-706.
- Kondo, R., Tadano, Y., Shizawa, K., 2014. A phase-field model of twinning and detwinning coupled with dislocation-based crystal plasticity for HCP metals. *Computational Materials Science* 95, 672-683.
- Liu, C., Shanthraj, P., Diehl, M., Roters, F., Dong, S., Dong, J., Ding, W., Raabe, D., 2018. An integrated crystal plasticity-phase field model for spatially resolved twin nucleation, propagation, and growth in hexagonal materials. *International Journal of Plasticity* 106, 203-227.
- Lou, C., Zhang, X., Ren, Y., 2015. Non-Schmid-based {10-12} twinning behavior in polycrystalline magnesium alloy. *Materials Characterization* 107, 249-254.
- Ma, Q., El Kadiri, H., Oppedal, A., Baird, J., Li, B., Horstemeyer, M., Vogel, S., 2012. Twinning effects in a rod-textured AM30 Magnesium alloy. *International Journal of Plasticity* 29, 60-76.
- Nolze, G., Hielscher, R., 2016. Orientations—perfectly colored. *Journal of Applied Crystallography* 49, 1786-1802.
- Pandey, A., Kabirian, F., Hwang, J.-H., Choi, S.-H., Khan, A.S., 2015. Mechanical responses and deformation mechanisms of an AZ31 Mg alloy sheet under dynamic and simple shear deformations. *International Journal of Plasticity* 68, 111-131.
- Papazafeiropoulos, G., Muñoz-Calvente, M., Martínez-Pañeda, E., 2017. Abaqus2Matlab: A suitable tool for finite element post-processing. *Advances in Engineering Software* 105, 9-16.
- Paramatmuni, C., Kanjarla, A.K., 2018. A crystal plasticity FFT based study of deformation twinning, anisotropy and micromechanics in HCP materials: Application to AZ31 alloy. *International Journal of Plasticity*.
- Proust, G., Tomé, C.N., Jain, A., Agnew, S.R., 2009. Modeling the effect of twinning and detwinning during strain-path changes of magnesium alloy AZ31. *International Journal of Plasticity* 25, 861-880.
- Qiao, H., Agnew, S., Wu, P., 2015. Modeling twinning and detwinning behavior of Mg alloy ZK60A during monotonic and cyclic loading. *International Journal of Plasticity* 65, 61-84.
- Quey, R., Dawson, P., Barbe, F., 2011. Large-scale 3D random polycrystals for the finite element method: Generation, meshing and remeshing. *Computer Methods in Applied Mechanics and Engineering* 200, 1729-1745.
- Salvati, E., Korsunsky, A.M., 2017. An analysis of macro- and micro-scale residual stresses of Type I, II and III using FIB-DIC micro-ring-core milling and crystal plasticity FE modelling. *International Journal of Plasticity* 98, 123-138.
- Shi, Z.-Z., Zhang, Y., Wagner, F., Juan, P.-A., Berbenni, S., Capolungo, L., Lecomte, J.-S., Richeton, T., 2015. On the selection of extension twin variants with low Schmid factors in a deformed Mg alloy. *Acta Materialia* 83, 17-28.
- Taylor, G.I., 1938. Plastic strain in metals. *J. Inst. Metals* 62, 307-324.
- Wang, F., Agnew, S.R., 2016. Dislocation transmutation by tension twinning in magnesium alloy AZ31. *International Journal of Plasticity* 81, 63-86.
- Wang, H., Wu, P.D., Tomé, C.N., Wang, J., 2012. A constitutive model of twinning and detwinning for hexagonal close packed polycrystals. *Materials Science and Engineering: A* 555, 93-98.
- Wang, H., Wu, P.D., Wang, J., Tomé, C.N., 2013. A crystal plasticity model for hexagonal close packed (HCP) crystals including twinning and de-twinning mechanisms. *International Journal of Plasticity* 49, 36-52.

- Wang, L., Huang, G., Quan, Q., Bassani, P., Mostaed, E., Vedani, M., Pan, F., 2014. The effect of twinning and detwinning on the mechanical property of AZ31 extruded magnesium alloy during strain-path changes. *Materials & Design* 63, 177-184.
- Wonsiewicz, B.C., 1966. *Plasticity of magnesium crystals*. Massachusetts Institute of Technology.
- Wu, L., Agnew, S.R., Brown, D.W., Stoica, G.M., Clausen, B., Jain, A., Fielden, D.E., Liaw, P.K., 2008. Internal stress relaxation and load redistribution during the twinning-detwinning-dominated cyclic deformation of a wrought magnesium alloy, ZK60A. *Acta Materialia* 56, 3699-3707.
- Wu, W., Lee, S.Y., Paradowska, A.M., Gao, Y., Liaw, P.K., 2012. Twinning-detwinning behavior during fatigue-crack propagation in a wrought magnesium alloy AZ31B. *Materials Science and Engineering: A* 556, 278-286.
- Xin, Y., Zhou, X., Chen, H., Nie, J.-F., Zhang, H., Zhang, Y., Liu, Q., 2014. Annealing hardening in detwinning deformation of Mg-3Al-1Zn alloy. *Materials Science and Engineering: A* 594, 287-291.
- Yin, S., Yang, F., Yang, X., Wu, S., Li, S., Li, G., 2008. The role of twinning-detwinning on fatigue fracture morphology of Mg-3% Al-1% Zn alloy. *Materials Science and Engineering: A* 494, 397-400.
- Zhang, H., Fong, K.S., Song, X., Ying, S., Salvati, E., Sui, T., Korsunsky, A.M., 2016. Synchrotron X-ray Diffraction Analysis of Bending Strains in Magnesium Alloy AZ31B Processed by Severe Plastic Deformation, *Proceedings of the International MultiConference of Engineers and Computer Scientists*. Newswood Limited, Hong Kong, pp. 685-690.
- Zhang, H., Liu, J., Sui, D., Cui, Z., Fu, M.W., 2018. Study of microstructural grain and geometric size effects on plastic heterogeneities at grain-level by using crystal plasticity modeling with high-fidelity representative microstructures. *International Journal of Plasticity* 100, 69-89.